Inverse cascades and α effect at a low magnetic Prandtl number

P. D. Mininni
NCAR, P.O. Box 3000, Boulder, Colorado 80307-3000, USA

(Received 13 February 2007; revised manuscript received 25 June 2007; published 24 August 2007)

Dynamo action in a fully helical Arn'old-Beltrami-Childress flow is studied using both direct numerical simulations and subgrid modeling. Sufficient scale separation is given in order to allow for large-scale magnetic energy buildup. Growth of magnetic energy obtains down to a magnetic Prandtl number $P_M=R_M/R_V$ close to 0.005, where R_V and R_M are the kinetic and magnetic Reynolds numbers. The critical magnetic Reynolds number for dynamo action R_M^c seems to saturate at values close to 20. Detailed studies of the dependence of the amplitude of the saturated magnetic energy with P_M are presented. When P_M is decreased, numerical experiments are conducted with either R_V or R_M kept constant. In the former case, the ratio of magnetic to kinetic energy saturates to a value slightly below unity as P_M decreases. Examination of energy spectra and structures in real space reveals that quenching of the velocity by a large-scale magnetic field takes place, with an inverse cascade of magnetic helicity and a force-free field at large scale in the saturated regime.

DOI: 10.1103/PhysRevE.76.026316 PACS number(s): 47.65.−d, 47.27.E−, 91.25.Cw, 95.30.Qd

I. INTRODUCTION

In recent years the increase in computing power, as well as the development of subgrid models for magnetohydrodynamic (MHD) turbulence [1–5] has allowed the study of a numerically almost unexplored territory: the regime of low magnetic Prandtl number ($P_M=R_M/R_V$, where R_V and R_M are, respectively, the kinetic and magnetic Reynolds numbers). This MHD regime is of particular importance since several astrophysical [6] and geophysical [7,8] problems are characterized by $P_M<1$, such as, for example, in the liquid core of planets, such as Earth, or in the convection zone of solar-type stars. Also, liquid metals (e.g., mercury, sodium, and gallium) used in the laboratory in attempting to generate dynamo magnetic fields are in this regime [9–13].

In recent publications [14–18], driven turbulent MHD dynamos were studied numerically within the framework of rectangular periodic boundary conditions. As P_M is lowered at fixed viscosity, the magnetofluid becomes more resistive than it is viscous, and it was found that magnetic fields were harder to excite by the dynamo process because of the increased turbulence in the fluid. The principal result was in obtaining the dependence of the critical magnetic Reynolds number R_M^c with the magnetic Prandtl number. These studies were done for several settings, ranging from coherent helical [18] and nonhelical [15,17] forcing, as well as for random forcing [14,16,19] (see also [20,21] for theoretical arguments based on the Kazantsev model [22]). In all cases, an asymptotic regime was found at small values of P_M.

For coherent forcing such as the Taylor-Green vortex (which corresponds to several laboratory experiments using two counterrotating disks), the value of R_M^c was observed to increase by a factor larger than 6 before the asymptotic regime for small values of P_M was reached [15]. Although the precise value of R_M^c in experiments is expected to be modified by the presence of boundaries, it is of interest to study what properties of the forcing can modify and decrease its value. It is well known from theory [23], two-point closure models [24], and direct numerical simulations (DNSs) at $P_M=1$ [25–27] that the presence of net helicity in the flow helps the dynamo and decreases the value of R_M^c.

In [18] dynamos with a helical forcing function were studied using the Roberts flow, but mechanical energy was injected at a wave number $|\mathbf{k}|=\sqrt{2}$, which left no room in the spectrum for any back-transfer of magnetic helicity as expected in the helical case [24,28,29] (the computations were done in a box of length 2π corresponding to a $k=1$ gravest mode). Indeed, the magnetic energy spectrum in these simulations peaked at scales smaller than the forcing scale at all times. In this work, in contrast, we study the effect of a fully helical Arn'old-Beltrami-Childress (ABC) forcing [30] with energy injected at a slightly smaller scale (note that the ABC forcing is related to the Roberts forcing, since it can be defined as a superposition of three Roberts flows). As a result of the intermediate-scale forcing, some α effect or inverse cascade of magnetic helicity can *a priori* develop and a magnetic field at scales larger than the forcing scale can grow.

ABC flows and helical dynamos were explored in many different contexts in the literature (see, e.g., [31] for a study close to $P_M=1$ and [32,33] for studies in the context of fast dynamo action). The main aim of the present work is to study the impact of helical flows at intermediate scales in the development of magnetic fields through dynamo action at $P_M<1$. In this context, it is worth noting that some simulations of ABC dynamos in the low-magnetic-Prandtl-number regime were discussed in [27,34], although no systematic exploration of the space of parameters was attempted. Also, Ref. [35] presented some preliminary results for the kinematic dynamo regime with ABC forcing. In this work we will focus on a study of the generation of large-scale magnetic fields and of the nonlinear saturation regime. A similar study was recently conducted in [36] using mean-field theory [28,29] and shell models. In this paper, we attempt to systematically study the saturation values of the fields for helical flows at $P_M<1$ in numerical simulations.

II. DEFINITIONS AND METHODOLOGY

In a familiar set of dimensionless ("Alfvénic") units the equations of magnetohydrodynamics are

$$\frac{\partial \mathbf{v}}{\partial t} + \mathbf{v}\cdot\nabla\mathbf{v} = -\nabla\mathcal{P} + \mathbf{j}\times\mathbf{B} + \nu\nabla^2\mathbf{v} + \mathbf{f}, \quad (1)$$

$$\frac{\partial \mathbf{B}}{\partial t} + \mathbf{v}\cdot\nabla\mathbf{B} = \mathbf{B}\cdot\nabla\mathbf{v} + \eta\nabla^2\mathbf{B}, \quad (2)$$

with $\nabla\cdot\mathbf{v}=\nabla\cdot\mathbf{B}=0$. Here, $\mathbf{v}$ is the velocity field, regarded as incompressible, and $\mathbf{B}$ is the magnetic field, related to the electric current density $\mathbf{j}$ by $\mathbf{j}=\nabla\times\mathbf{B}$. $\mathcal{P}$ is the pressure, obtained by solving the Poisson equation that results from taking the divergence of Eq. (1) and using the incompressibility condition $\nabla\cdot\mathbf{v}=0$. The viscosity ν and magnetic diffusivity η define mechanical Reynolds numbers and magnetic Reynolds numbers, respectively, as $R_V=LU/\nu$ and $R_M=LU/\eta$. Here U is a typical turbulent flow speed (the rms velocity in the following sections, $U=\langle u^2\rangle^{1/2}$, with the brackets denoting spatial averaging) and L is a length scale associated with spatial variations of large-scale flow (the integral length scale of the flow).

Some global quantities will appear repeatedly in the next sections. These are the total energy (the sum of the kinetic E_V and magnetic E_M energies) $E=E_V+E_M=\frac{1}{2}\int(\mathbf{u}^2+\mathbf{B}^2)dV$, the magnetic helicity $H_M=\int\mathbf{A}\cdot\mathbf{B}\,dV$ (where $\mathbf{A}$ is the vector potential, defined such as $\mathbf{B}=\nabla\times\mathbf{A}$), the current helicity $H_J=\int\mathbf{B}\cdot\mathbf{j}\,dV$, and the kinetic helicity $H_V=\int\mathbf{v}\cdot\boldsymbol{\omega}\,dV$ (where $\boldsymbol{\omega}=\nabla\times\mathbf{v}$ is the vorticity). While E and H_M are ideal ($\nu=\eta=0$) quadratic invariants of the MHD equations, H_J and H_V are not. In practice, kinetic helicity in helical dynamos is injected into the flow by the mechanical forcing $\mathbf{f}$ (e.g., by rotation and stratification in geophysical and astrophysical flows [23]). We define also the kinetic and magnetic energy dissipation rates, respectively, as $\epsilon_V=\nu\langle\boldsymbol{\omega}^2\rangle$ and $\epsilon_M=\eta\langle\mathbf{j}^2\rangle$.

Equations (1) and (2) are solved numerically using a parallel pseudospectral code, as described in [17,18]. We impose rectangular periodic boundary conditions throughout, using a three-dimensional box of edge 2π. The integral and Taylor scales are defined, respectively, as

$$L = 2\pi\sum_{\mathbf{k}} k^{-1}|\hat{\mathbf{v}}(\mathbf{k})|^2 \Big/ \sum_{\mathbf{k}} |\hat{\mathbf{v}}(\mathbf{k})|^2, \quad (3)$$

$$\lambda = 2\pi\left(\sum_{\mathbf{k}} |\hat{\mathbf{v}}(\mathbf{k})|^2 \Big/ \sum_{\mathbf{k}} k^2|\hat{\mathbf{v}}(\mathbf{k})|^2\right)^{1/2}, \quad (4)$$

where $\hat{\mathbf{v}}(\mathbf{k})$ is the amplitude of the mode with wave vector $\mathbf{k}$ ($k=|\mathbf{k}|$) in the Fourier transform of $\mathbf{v}$. Using the Taylor length scale, we can also define a Taylor-based Reynolds number $R_\lambda=\lambda U/\nu$.

The external forcing function $\mathbf{f}$ in Eq. (1) injects both kinetic energy and kinetic helicity. For $\mathbf{f}$ we use the ABC flow

$$\mathbf{f}_{\mathrm{ABC}} = f_0\{[B\cos(k_F y) + C\sin(k_F z)]\hat{x} + [C\cos(k_F z) + A\sin(k_F x)]\hat{y} + [A\cos(k_F x) + B\sin(k_F y)]\hat{z}\}, \quad (5)$$

with $A=0.9$, $B=1$, $C=1.1$ [34], and $k_F=3$. The ABC flow is an eigenfunction of the curl with eigenvalue k_F, and as a result, if used as an initial condition, it is an exact solution of the Euler equations. In the hydrodynamic simulations, for large enough ν (small R_V) the laminar solution is stable. As ν is decreased the laminar flow becomes unstable and develops turbulence (see [37] for a study of early bifurcations at intermediate Reynolds numbers).

To properly resolve the turbulent flow, the maximum wave number in the code, $k_{\max}=N/3$ (N is the linear resolution and the standard 2/3-rule for de-aliasing is used), has to be larger than the mechanical dissipation wave number $k_\nu=(\epsilon_V/\nu^3)^{1/4}$. As a result, as ν decreases and R_V increases, the linear resolution N has to be increased. At some point the use of DNSs to solve Eqs. (1) and (2) turns out to be too expensive from a computational point of view and some kind of model for unresolved scales is needed.

To extend the range of R_V and P_M studied, we use the Lagrangian-averaged MHD equations (LAMHD, also known as the MHD α model) [4,38,39]

$$\frac{\partial \mathbf{v}}{\partial t} + \mathbf{u}_s\cdot\nabla\mathbf{v} = -v_j\nabla u_s^j - \nabla\tilde{\mathcal{P}} + \mathbf{j}\times\mathbf{B}_s + \nu\nabla^2\mathbf{v} + \mathbf{f}, \quad (6)$$

$$\frac{\partial \mathbf{B}_s}{\partial t} + \mathbf{u}_s\cdot\nabla\mathbf{B}_s = \mathbf{B}_s\cdot\nabla\mathbf{u}_s + \eta\nabla^2\mathbf{B}. \quad (7)$$

In these equations, the pressure $\tilde{\mathcal{P}}$ is determined, as before, from the divergence of Eq. (6) and the incompressibility condition. The suffix s denotes smoothed fields, related to the unsmoothed fields by

$$\mathbf{v} = (1-\alpha_V^2\nabla^2)\mathbf{u}_s, \quad (8)$$

$$\mathbf{B} = (1-\alpha_M^2\nabla^2)\mathbf{B}_s, \quad (9)$$

where α_V and α_M are two filtering scales.

The total energy in this system is given by $E=E_V+E_M=\frac{1}{2}\int(\mathbf{v}\cdot\mathbf{u}_s+\mathbf{B}\cdot\mathbf{B}_s)dV$; it is one of the ideal quadratic invariants of the LAMHD equations. Equivalently, the magnetic helicity invariant is now given by $H_M=\int\mathbf{A}_s\cdot\mathbf{B}_s\,dV$, where the smooth vector potential is defined such as $\mathbf{B}_s=\nabla\times\mathbf{A}_s$. The current helicity is given by $H_J=\int\mathbf{B}_s\cdot\mathbf{j}\,dV$. The expression for the kinetic helicity is the same in MHD and LAMHD, and the dissipation rates in LAMHD are $\epsilon_V=\nu\langle\boldsymbol{\omega}\cdot\boldsymbol{\omega}_s\rangle$ and $\epsilon_M=\eta\langle\mathbf{j}^2\rangle$, where $\boldsymbol{\omega}_s=\nabla\times\mathbf{u}_s$ [5].

The LAMHD equations are a regularization of the MHD equations, and as a result, they allow for simulations of turbulent flows at a given Reynolds number using a lower resolution than in DNSs. This subgrid model was tested against DNSs of MHD flows in [4,5]. As in previous studies of dynamo action at low P_M, the ratio of the two filtering scales α_V and α_M was set using the ratio of the kinetic and magnetic dissipation scales—i.e., $\alpha_V/\alpha_M=P_M^{3/4}$ [15]. The value of α_V depends on the linear resolution and was adjusted to $1/\alpha_V\approx k_{\max}/2$ [40].

In the next section, we describe the computations and the results for both the kinematic dynamo regime [where $\mathbf{j}\times\mathbf{B}$ is negligible in Eq. (1)] and for full MHD (where the Lorentz force modifies the flow). The first step is to establish what are the thresholds in R_M at which dynamo behavior sets in as R_V is raised and P_M is decreased (Sec. III A). The procedure to do this is the following (see, e.g., [15]). First a hydrodynamic simulation at a given value of R_V is done. Then, a

TABLE I. Parameters for the simulations: kinematic viscosity ν, Taylor Reynolds number R_λ, mechanical Reynolds number R_V, range of values of the magnetic Reynolds number R_M for a given flow, linear resolution N, and value of the mechanical filter length α_V (with $\alpha_V/\alpha_M=[R_M/R_V]^{3/4}$ in each case). For direct simulations (no subgrid model), α_V need not be defined. Runs in set 6a have the same values of parameters as in set 6, but a subgrid model at a lower resolution was used. Run 9 has the same parameters as set 9b with $R_M=41$, but was done using a DNS. The lowest P_M achieved for this set of runs is ≈ 0.005.

Set	ν	R_λ	R_V	R_M	N	α_V
1	0.2	11	11	9–16	64	
2	0.1	21	23	10–19	64	
3	4×10^{-2}	55	71	17–71	64	
4	9×10^{-3}	161	240	18–54	64	
5	4×10^{-3}	250	450	15–450	128	
6	2×10^{-3}	360	820	10–41	256	
6a	2×10^{-3}	290	840	10–41	64	0.1
7	1×10^{-3}	340	1700	14–42	128	0.0625
8	6.2×10^{-4}	680	2500	39	512	
9	5×10^{-4}	500	3400	41	512	
9b	5×10^{-4}	500	3400	14–42	256	0.03125
10	2.5×10^{-4}	1100	6200	77	1024	

small and random (nonhelical) magnetic field is introduced and several simulations are done changing only the value of R_M. At a given R_M, the magnetic energy can either decay or grow exponentially. In each simulation, the magnetic energy growth rate σ is then defined as $\sigma=d\ln(E_M)/dt$ (note that with this definition, σ is twice the growth rate of the magnetic field **B**). The critical magnetic Reynolds number R_M^c for the onset of dynamo action corresponds to $\sigma=0$ and, in practice, is obtained from a linear interpolation between the two points with, respectively, positive and negative σ closest to zero. The growth rate σ is typically expressed in units of the reciprocal of the large-scale eddy turnover time $T=L/U$.

Once the values of R_M^c for different values of $P_M\leq 1$ have been found, simulations for $R_M>R_M^c$ are conducted for longer times (Sec. III B). In this case, magnetic fields are initially amplified exponentially and then saturate due to the back reaction of the magnetic field on the flow. In helical flows, this saturation is accompanied by the growth of magnetic fields in the largest scale available in the box. In this regime, we will study the maximum value attained by the magnetic energy as a function of P_M (Sec. III C), as well as the amount of magnetic energy at scales larger than the forcing scale (Sec. III D). Note that, while the determination of R_M^c described above is done (for computational reasons) varying R_M while keeping R_V fixed, in the nonlinear regime simulations are done following the same procedure, but also varying R_V while keeping R_M constant. Different results are obtained depending on the way the space of parameters is explored. Asymptotic regimes are found for the latter case, but the former case is also discussed here since it is often considered in numerical explorations. Finally, Sec. IV is the conclusion.

III. SIMULATIONS AND RESULTS

In order to obtain a systematic study of dynamo action for ABC forcing and $P_M\leq 1$, a suite of several simulations was conducted. Table I shows the parameters used in the simulations. Note that when a range is invoked in the values of R_M, it indicates several runs were done with the same value of R_V, but changing the value of R_M to span the range (typically three to five runs). The set of runs 6 and 6a have the same parameters (ν, η, and rms velocity), but while set 6 comprises DNSs at resolutions of 256^3 grid points, in set 6a the spatial resolution is 64^3 and the LAMHD equations were used in order to further the testing of the model. Similar considerations apply to run 9 and set 9b.

A. Threshold for dynamo action

Figure 1 summarizes the results of the study of the dependence of the threshold R_M^c as P_M is decreased. For values of R_M above the curve, dynamo action takes place and initially small magnetic fields are amplified. Below the curve, Ohmic dissipation is too large to sustain a dynamo. Noteworthy is the qualitative similarity of the curve between the ABC flow and previous results using different mechanical forcings

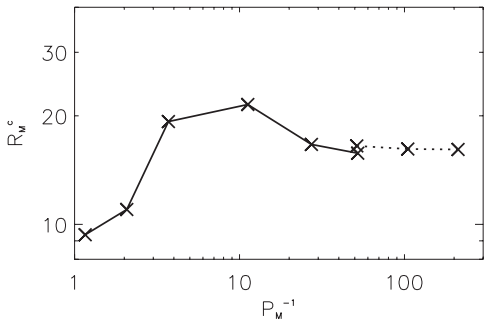

FIG. 1. Critical magnetic Reynolds R_M^c as a function of P_M^{-1}: DNSs (solid line) and LAMHD simulations (dotted line). Note the saturation for $P_M\leq 0.02$.

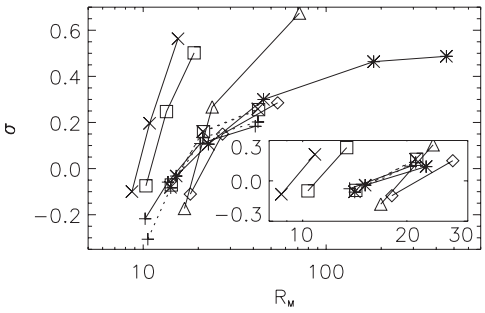

FIG. 2. Growth rates as a function of R_M. Each line corresponds to several simulations at constant R_V (fixed ν), and each point in the line indicates the exponential growth (or decay) rate at a fixed value of R_M. The point where each curve crosses $\sigma=0$ gives the threshold R_M^c for dynamo instability. Points from DNSs are connected with solid lines, and labels are the following: set 1 ($\times$), set 2 ($\square$), set 3 ($\triangle$), set 4 ($\diamond$), set 5 ($*$), and set 6 (+). Points from LAMHD simulations are connected with dotted lines: set 6a (+), set 7 ($\times$), and set 9b ($\square$). Note the accumulation of lines near $R_M \approx 20$. The inset shows the two points closer to $\sigma=0$ for each set of runs.

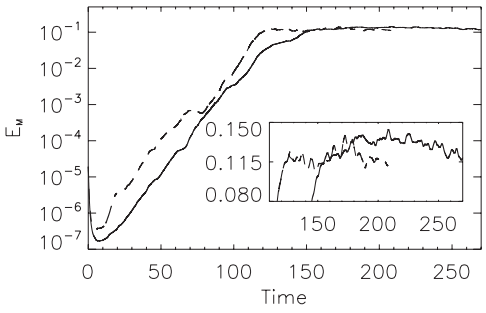

FIG. 3. Time history of the magnetic energy for runs in set 6 (dashed line) and in set 6a (solid line) with $R_M \approx 41$ and $P_M=5\times10^{-2}$. The inset shows the time evolution of the magnetic energy after saturation, in linear scale.

[15,17–19]. Namely, an increase in R_M^c is observed as turbulence develops, and then an asymptotic regime is found in which the value of R_M^c is independent of P_M. Note that LAMHD simulations were used to extend the study for values of P_M smaller than what can be studied using DNSs. Simulations at the same value of P_M were carried out with the two methods to compare the results (sets 6 and 6a). This procedure was used before in [15]. As in the previous study, the LAMHD equations slightly overestimate the value of R_M^c.

Besides the similarities in the shape of the curves for different forcing functions, two quantitative differences are striking: (i) only a mild rise in R_M^c is observed here as P_M is decreased (a factor of 2, while a factor larger than 6 obtains for the Taylor-Green vortex [15] and a factor larger than 5 for random forcing [19]) and (ii) the asymptotic value of R_M^c for small values of P_M is 10 times smaller than for other flows studied [15,18,19]. A similar result was obtained using mean-field theory and shell models in [36], and the quantitative differences observed were associated with the relative ease to excite large-scale helical dynamos compared with nonhelical and small-scale dynamos.

Note that the curve in Fig. 1 was constructed using sets 1–7 and 9b of Table I. Several runs at constant R_V but varying R_M are required to define R_M^c. Set 9b reveals a dynamo at the lowest magnetic Prandtl number known today in numerical simulations: namely, $P_M=4.7\times10^{-3}$.

Figure 2 shows the details of how the thresholds for the determination of the $R_M^c=f(P_M^{-1})$ curve were calculated. For small initial E_M, broadly distributed over a set of wave numbers, η was decreased in steps to raise R_M in the same mechanical setting until a value of $\sigma\approx0$ was identified. A linear fit between the two points with σ closest to $0^{\pm}$ provides a single point on the curves in Fig. 1. Note that Fig. 2 also gives bounds for the uncertainties in the determination of the threshold R_M^c (see, e.g., [15]): errors in Fig. 1 can be defined as the distance between the value of R_M^c and the value of R_M in the simulation with σ closest to 0. Note also the asymptotic approach to a growth rate of order unity for large values of the magnetic Reynolds number, such as, for example, in the runs in set 5.

B. Time evolution

1. Comparison of MHD and LAMHD

A comparison of the time evolution of the magnetic energy in two dynamo runs with the same magnetic Reynolds and Prandtl numbers ($R_M\approx41$, $P_M=5\times10^{-2}$) is shown in Fig. 3. One of the runs is a DNS from set 6, while the other is a LAMHD simulation from set 6a. Two different stages can be identified at first sight in these runs: the kinematic regime at early times, with an exponential amplification of the magnetic energy (used to define the growth rates and thresholds in Figs. 1 and 2), and the saturated regime at late times. As expected from the results discussed in the previous subsection, the LAMHD equations at a coarser grid (64^3) are able to capture the kinematic dynamo regime. While in DNSs with a resolution of 256^3 the growth rate is $\sigma\approx0.18$, in the LAMHD simulation $\sigma\approx0.20$. But the LAMHD simulation also captures properly the saturation (albeit the saturated level is reached a bit earlier) and the amplitudes of the magnetic energy in the steady state are comparable (see inset in Fig. 3). Small differences observed in the time evolution are likely due to differences in the initial random magnetic seed. In the following, we shall use both DNS and LAMHD simulations to study the saturated regime at low P_M.

2. Time evolution for R_V fixed

In helical flows, as magnetic energy saturates, a large-scale magnetic field develops (i.e., at scales larger than the forcing scale) due to the helical α effect [23,24,27–29,41]. It is of interest to know what happens with the amplitude of the magnetic field as the value of P_M is decreased. An example is shown in Fig. 4, which gives the magnetic energy as a function of time for runs in set 5. Only the value of R_M (and therefore of P_M) is changed between the runs ($R_V\approx450$ in all runs and P_M varying from 1 to 0.03). For large values of R_M (but not necessarily for values of P_M close to unity), the growth rate σ is independent of R_M and of order 1 as noted in Sec. III A. Furthermore, as P_M is decreased, both σ and the

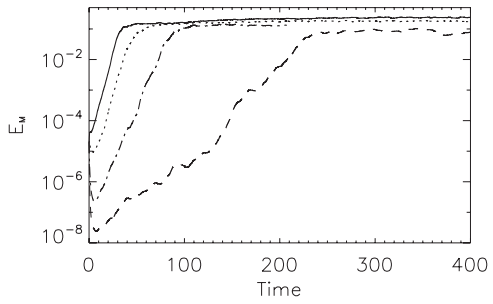

FIG. 4. Time history of the magnetic energy for runs in set 5 (constant $R_V \approx 450$). The magnetic Reynolds numbers of the runs are $R_M \approx 22$ (dashed line), $R_M \approx 45$ (dashed-dotted line), $R_M \approx 180$ (dotted line), and $R_M \approx 450$ (solid line).

saturation value of the magnetic energy decrease. However, for the lowest value of P_M studied here, the magnetic Reynolds number is quite low and close to R_M^c. In that context, computations varying P_M while keeping R_M constant are useful to see what fraction of the present result is a threshold effect when R_M is close to R_M^c.

Figure 5 shows the evolution of the magnetic helicity as a function of time for the same simulations as in Fig. 4. The external forcing injects positive kinetic helicity in the flow. In the kinematic regime, the α effect is proportional to minus the kinetic helicity [28,29]. From mean-field theory, the magnetic field in the large scales should grow with magnetic helicity of the same sign as the α effect (negative), as indeed observed (see [27,42] for helical dynamo simulations at $P_M = 1$). In the simulations, magnetic helicity grows exponentially during the kinematic regime. In runs with small R_M, the saturated state is reached shortly after the saturation of the exponential phase. But as R_M is increased, it is now clear that an intermediate stage develops in which magnetic energy and helicity keep growing slowly. As a result, saturation takes place in longer times and the time to reach the final steady state depends on the large-scale magnetic diffusion time ($T_\eta \approx 4\pi^2/\eta$). The dependence of the saturation time with R_M can be observed in Fig. 5. It is also worth mentioning that even in the runs with $P_M < 1$, the saturation of magnetic helicity can be well described by the formula $H_M(t) = H_0(k_F/k_0)^2\{1-\exp[-2\eta k_0^2(t-t_{\rm sat})]\}$, where $k_0 = 1$ is the

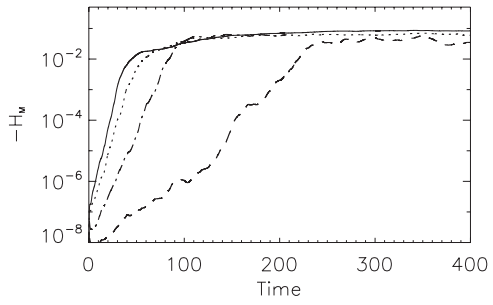

FIG. 5. Time history of (minus) the magnetic helicity for runs in set 5 (constant $R_V \approx 450$). The magnetic Reynolds numbers of the runs are $R_M \approx 22$ (dashed line), $R_M \approx 45$ (dashed-dotted line), $R_M \approx 180$ (dotted line), and $R_M \approx 450$ (solid line).

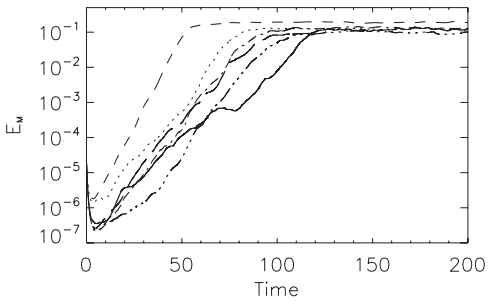

FIG. 6. Time history of the magnetic energy in simulations at constant $R_M \approx 41$ ($\eta = 4 \times 10^{-2}$). The different runs are taken from set 3 ($P_M = 1$, dashed line), set 4 ($P_M = 0.225$, dotted line), set 5 ($P_M = 0.1$, dash-dotted line), set 6 ($P_M = 0.05$, solid line), set 7 ($P_M = 0.025$, dash–triple-dotted line), and finally set 9 ($P_M = 0.0125$, long-dashed line).

gravest mode, $H_0(k_F/k_0)^2$ is the saturation amplitude of the magnetic helicity at late times, and $t_{\rm sat}$ is the saturation time of the small-scale magnetic field [27] [the formula approximates the evolution of $H_M(t)$ only for $t > t_{\rm sat}$, after the growth of the small-scale magnetic field saturates]. This result indicates that the slow saturation of the dynamo is dominated by the evolution of the magnetic helicity in the largest scale in the system (note that the formula describes the late saturation of the magnetic helicity, dominated by its large scale component).

3. Time evolution for R_M fixed

From Figs. 4 and 5 it seems apparent that small values of P_M have a negative impact on the amplitude of the magnetic field generated by the dynamo. However, different results are obtained when the space of parameters is explored keeping R_M constant and increasing R_V, as another way to decrease P_M. Figure 6 shows the results in this case for the time evolution of the magnetic energy. As R_V is increased from small values, a drop in the growth rate σ and in the saturation value of the magnetic energy is observed. But then an asymptotic regime is reached, in which both σ and the saturation value seem to be roughly independent of R_V and P_M. As a result, we conclude that the behavior observed in Figs. 4 and 5 is the result of a critical slowing down: if the space of parameters is explored at constant R_V, as P_M is decreased, R_M gets closer to R_M^c until no dynamo action is possible. On the other hand, all the simulations with $P_M \leq 0.05$ shown in Fig. 5 have R_M/R_M^c approximately constant (see Fig. 1) and a critical slowing down is not observed.

C. Saturation values

The amplitude of the magnetic energy (normalized by the kinetic energy) as a function of the magnetic Prandtl number after saturation takes place is shown in Fig. 7. This figure summarizes the results discussed in Figs. 4 and 6. As the value of P_M is decreased, if R_V is kept constant and R_M (and thus P_M) decreases, the saturation of the dynamo takes place for lower values of the magnetic energy. This is to be expected since as we decrease P_M we also decrease R_M and at

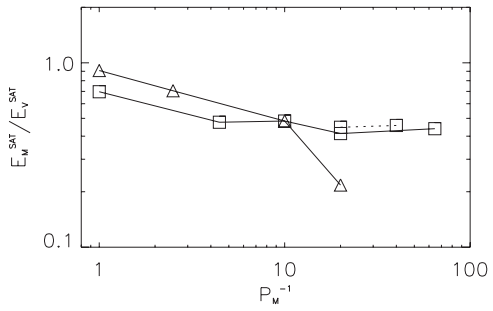

FIG. 7. Saturation value of the magnetic energy (normalized by the kinetic energy in the saturated regime). The triangles correspond to simulations at constant R_V, while the squares correspond to simulations at constant R_M (squares connected with solid lines are from DNSs, while squares connected with dotted lines are from LAMHD simulations). Note the saturation at low P_M for constant R_M runs.

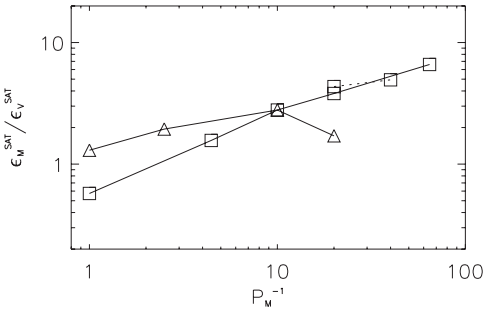

FIG. 8. Saturation value of the magnetic dissipation rate normalized by the kinetic energy in the saturated regime. The triangles correspond to simulations at constant R_V, while the squares correspond to simulations at constant R_M (squares connected with solid lines are from DNSs, while squares connected with dotted lines are from LAMHD simulations).

some point R_M^c is reached. It is not clear whether such a strong dependence would be observed if the constant R_V runs were performed at substantially higher values of R_V as found in astronomical bodies and in the laboratory; however, such runs would be quite demanding from a numerical standpoint unless one resorts to large-eddy-simulation (LES) techniques, few of which have been developed in MHD (see, e.g., [1–3]). For values of R_M smaller than R_M^c, no dynamo action is expected and the ratio E_M/E_V should indeed go to zero. On the other hand, in the simulations with constant R_V, the ratio E_M/E_V seems to saturate for $P \lesssim 0.25$ and reach an approximately constant value close to ≈ 0.5. This indicates that small-scale turbulent fluctuations in the velocity field are strongly quenched by the large-scale magnetic field, as will be also shown later in the spectral evolution of the energies. The ratio E_M/E_V in helical large-scale dynamos is also expected to be dependent on the scale separation between the forcing wave number (here fixed to $k_F=3$) and the largest wave number in the system (here $k=1$). As the scale separation increases and there is more space for an inverse cascade of magnetic helicity, we expect the ratio E_M/E_V in the $P_M < 1$ regime to also increase.

Figure 8 shows the ratio of the magnetic energy dissipation rate ϵ_M to the kinetic energy dissipation rate ϵ_V in the saturated state for the same runs as in Fig. 7. At constant R_V, for small values of P_M, a drop in the ratio is observed as the value of R_M gets closer to the threshold. On the other hand, at constant R_M, more and more energy is dissipated by Ohmic dissipation as P_M is decreased.

D. Spectral evolution

1. Kinetic and magnetic energy

In [17,18] it was shown using different forcing functions that even at low P_M the magnetic energy spectrum in the kinematic regime of the dynamo peaks at small scales. In these simulations, the critical magnetic Reynolds number R_M^c was of the order of a few hundreds, and as a result, small scales were excited. For ABC forcing, R_M^c is of the order of a few tens and close to the threshold small scales are damped fast. Only large-scale dynamo action is observed and thus, even at early times, the magnetic energy spectrum peaks at large scales. However, if R_M is increased above $R_M \approx 400$, a magnetic energy spectrum that peaks at scales smaller than the forcing scale (as in [17,18]) is recovered. We focus here on large-scale dynamo action and, as a result, will discuss the spectral evolution in simulations with R_M of a few tens.

Figure 9 shows the evolution of the magnetic energy spectrum at different times for a run in set 6 with $R_M \approx 41$ ($P_M = 0.05$). As in previous studies, in the kinematic regime all Fourier shells grow with the same rate. Then, magnetic saturation in the small scales is reached, while the $k=1$ shell keeps growing until it eventually saturates itself. Figure 10 shows the kinetic and magnetic energy spectra at late times ($t=210$) after saturation at all scales. At $k=1$ the system is dominated by magnetic energy, but at smaller scales the magnetic energy spectrum drops fast. The kinetic energy spectrum peaks at the forcing band ($k=3$) and then drops with a slope compatible with k^{-3}. This drop is due to the action of the Lorentz force that removes mechanical energy from the $k=3$ shell to sustain the magnetic field at $k=1$ [43,44].

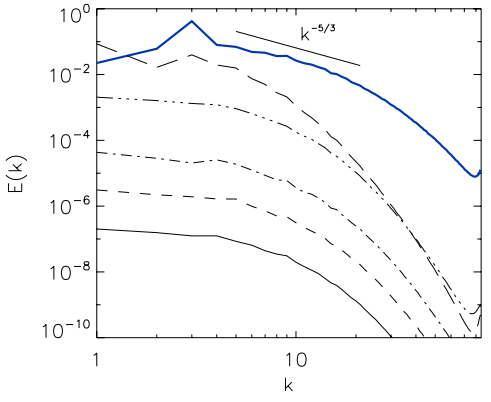

FIG. 9. (Color online) Kinetic energy spectrum at $t=0$ [thick (blue) lines], and magnetic energy spectrum (thin lines) at different times: $t=11$ (solid line), $t=29$ (dashed line), $t=47$ (dashed-dotted line), $t=95$ (dashed–triple-dotted line), and $t=120$ (long-dashed line). The spectra are for a run in set 6 with $R_M \approx 41$. The last time is in the saturation regime (see Fig. 6).

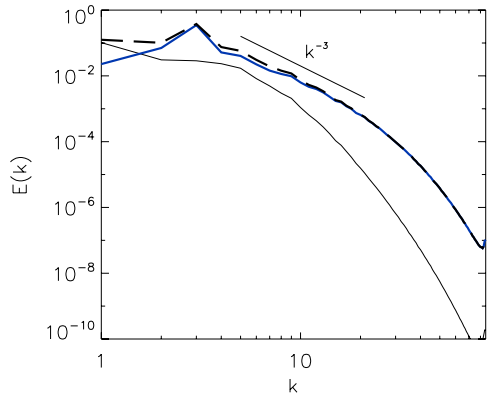

FIG. 10. (Color online) Kinetic [thick (blue) line] and magnetic energy spectra (thin line) at $t=210$ in the simulation in set 6 with $R_M \approx 41$ ($P_M=0.05$). The thick dashed line shows the total energy spectrum.

A slope close to a k^{-3} power law in the kinetic energy spectrum in the saturated regime at small scales is observed in several of the simulations with $P_M<1$. Simulations with small P_M and larger values of R_V were done using both the LAMHD equations and high-resolution DNSs on grids of 512^3 and 1024^3 points (see Table I). In these simulations, a power law close to $k^{-5/3}$ is observed before the kinetic energy spectrum drops to a steeper slope. As an example, Fig. 11 shows the kinetic and magnetic energy spectra in a simulation from set 9 using the LAMHD model, with $R_M \approx 41$ ($P_M=0.0125$). Slopes corresponding to $k^{-5/3}$, k^{-3}, and k^{-5} are indicated as a reference. A k^{-5} power law in the magnetic energy spectrum (following a k^{-3} range) was observed in experiments of dynamo action with constrained helical flows at low R_M [45]; in addition, a k^{-3} power law for the kinetic energy spectrum is consistent with the observed magnetic energy spectrum [46]. Note that these power laws are only discussed here in order to be able to compare with the experimental data, but higher Reynolds numbers and thus more resolution will be needed in order to ascertain the spectral dependence of the flow and the magnetic field in the different inertial ranges of low-P_M simulations.

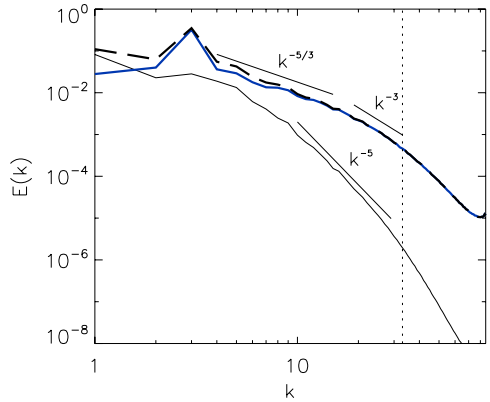

FIG. 11. (Color online) Kinetic [thick (blue) line] and magnetic energy spectra (thin line) at $t=150$ in the simulation in set 9 with $R_M \approx 41$ ($P_M=0.0125$) in the saturated regime. The thick dashed line shows the total energy spectrum and the thin vertical dotted line the wave number at which the α filtering sets in. Note the compatibility of the spectra with a Kolmogorov law in the large scales for the kinetic spectrum, followed by a steeper power law.

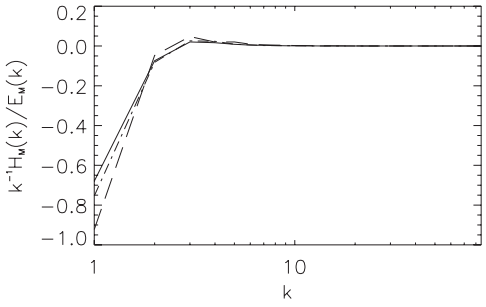

FIG. 12. Spectrum of relative magnetic helicity $k^{-1}H_M(k)/E_M(k)$ at different times in the simulation in set 6 with $R_M \approx 41$ ($P_M=0.05$). The labels are as in Fig. 9. Note the evolution toward a force-free field at $k=1$, the small excess of positive helicity at scales slightly smaller than the forcing scale, and the absence of relative magnetic helicity in the small scales at all times.

2. Helicities and inverse cascades

Figure 12 shows the spectrum of relative magnetic helicity $k^{-1}H_M(k)/E_M(k)$ at different times for the same run as in Figs. 9 and 10 (run with $R_M \approx 41$ in set 6). At all times, scales larger than the forcing scale have negative magnetic helicity, while scales of the order of, or smaller than, the forcing scale have positive magnetic helicity. This is consistent with an inverse cascade of negative magnetic helicity at wave numbers smaller than k_F and with a direct transfer of positive magnetic helicity at wave numbers larger than k_F, as analyzed in [47] using transfer functions. The relative helicity in the $k=1$ shell grows with time until reaching saturation. At late times, $H_M(k=1)/E_M(k=1) \approx -1$, indicating that the large-scale magnetic field is nearly force free. Note that a force-free field has maximum helicity and, from the Schwarz inequality $|H_M(k=1)/E_M(k=1)| \leq 1$, with the maximum value corresponding to the most helical case.

Figure 13 also shows the spectrum of $H_V(k)-k^2H_M(k)$, proportional to (minus) the nonlinear α effect [24]. Three times are shown for the same run as in Figs. 9, 10, and 12 (set 6, $R_M \approx 41$). At early times ($t=11$ and $t=29$) the spectrum of $H_V(k)-k^2H_M(k)$ is close to the spectrum of the kinetic helicity. However, as the large-scale magnetic field grows ($t=120$ is shown in the figure), the current helicity [$\sim k^2H_M(k)$ in the DNSs] quenches kinetic helicity fluctuations and the total spectrum drops at scales smaller than k_F.

As a result, at late times the magnetic energy is mostly in the modes with wave number $k=1$, which corresponds to the largest available scale in the system. In addition, the large-scale magnetic field is force free [maximum relative helicity with $H_M(k)=E_M(k)$ at $k=1$]. Figure 14 shows slices of the velocity and magnetic fields at early and late times. The growth at late times of a magnetic field at scales larger than the velocity field and the quenching of turbulent velocity fluctuations at small scales can be identified.

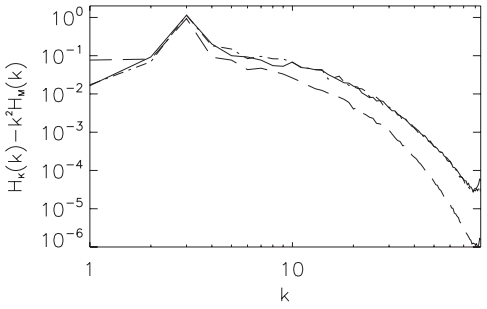

FIG. 13. Spectrum of $H_V(k)-k^2H_M(k)$, proportional to (minus) the nonlinear α effect, in the simulation in set 6 with $R_M \approx 41$ ($P_M=0.05$). The labels are as in Figs. 9 and 12: the solid line is for $t=11$, the dashed line for $t=29$, and the long dashed line for $t=120$. Note the drop of the spectrum at late times at scales smaller than k_F.

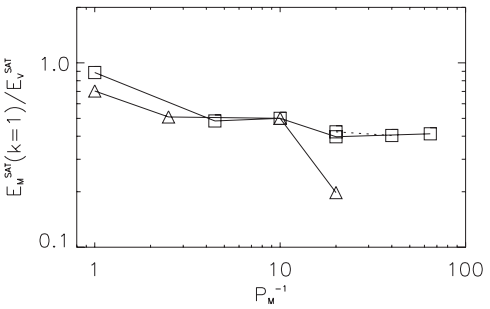

FIG. 15. Saturation value of the magnetic energy in the $k=1$ shell, normalized by the total kinetic energy. The triangles correspond to simulations at constant R_V, while the squares correspond to simulations at constant R_M (squares connected with solid lines are from DNSs, while squares connected with dotted lines are from LAMHD simulations).

The situation resembles other inverse-cascade situations that have been studied numerically, in which the fundamental $k=1$ mode dominates the dynamics at long times and its growth is only limited by its own dissipation rate [27,41,42,48]. In helical dynamo simulations at $P_M=1$ this behavior has also been observed, although it was speculated that for $P_M<1$ the inverse cascade of magnetic helicity and the generation of large-scale fields should be quenched [27]. In fact, the generation of magnetic energy at scales larger than the forcing scale is not quenched as P_M is decreased. This is further illustrated in Fig. 15, which shows the ratio of the magnetic energy in the $k=1$ shell to the total kinetic energy in the saturated state as a function of P_M. Curves both at constant R_V and constant R_M are given. For constant R_M and small P_M the magnetic energy in the large scales seems to be independent of P_M and R_V. The overall shape of the curves is similar to the curves in Fig. 7, indicating that at late times evolution of the total magnetic energy is dominated by the magnetic field at the largest available scale.

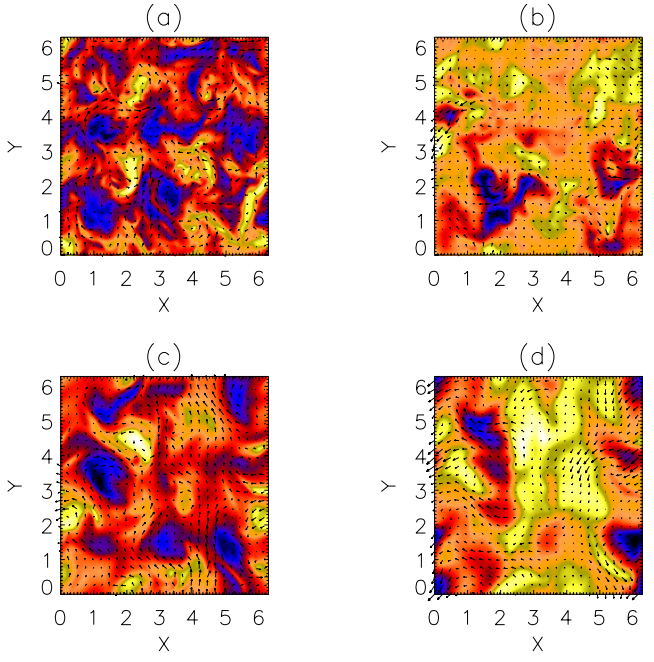

FIG. 14. (Color online) Plots of the velocity and magnetic fields in a cut at $z=0$ for the simulation in set 6 with $R_M \approx 41$ and $R_V \approx 820$ ($P_M=0.05$): (a) v_z component in color and v_x, v_y indicated by arrows at early time, (b) same as in (a) for the magnetic field at early time, (c) same as in (a) at late time, and (d) same as in (b) at late time.

IV. CONCLUSION

We have shown in this paper that the phenomenon of an inverse cascade of magnetic helicity, and the ensuing growth of large-scale magnetic energy together with a force-free magnetic field at large times, is present at low magnetic Prandtl number, down to $P_M=0.005$ in kinematic-regime studies and down to $P_M=0.01$ in simulations up to saturation. The quenching of the velocity in the small scales, already observed in laboratory experiments, is also present. Augmentation of the critical magnetic Reynolds number as R_V increases is less than in the nonhelical case [14–16] and even smaller than what was found for helical flows when the large-scale dynamo is not permitted, such as, e.g., for the Roberts flow at $k \approx 1$ [18]. The reason for this difference is that in the present study we allowed for enough scale separation between the forcing scale and the largest scale for helical large-scale dynamo action to develop. The results are in agreement with studies using mean-field theory and shell models to study both large- and small-scale dynamo actions [36]. Large-scale helical dynamo action in the $P_M<1$ regime requires much smaller magnetic Reynolds numbers to work than small-scale dynamos.

The challenge remains, numerically, to be able to reach values of the magnetic Prandtl number comparable to those found in geophysics and astrophysics and in the laboratory—i.e., $P_M \approx 10^{-5}$. However, it is unlikely that the dynamo instability found here down to $P_M=0.005$ would disappear as P_M is lowered further. An open question, of importance from the experimental point of view when dealing with turbulent liquid metals, is whether the critical magnetic Reynolds

number R_M^c will stabilize, for a given flow, at a value intermediate between what it is at $P_M=1$ and the peak of the curve (see Fig. 1) or whether, for large-scale helical dynamo action and extremely low values of P_M, it will go back down to the value it has at $P_M=1$. The data up to this day suggest the former, but on the other hand a study made in the context of two-point closures of turbulence [46] suggests the latter. This also means that reliable models of turbulent flows in MHD must be developed in order so that we can explore in a more systematic way the parameter-space characteristic of the flows of interest, as for the geodynamo or the solar dynamo.

ACKNOWLEDGMENTS

The author is grateful to D.C. Montgomery and A. Pouquet for valuable discussions and their careful reading of the manuscript. Computer time was provided by NCAR and by the National Science Foundation Terascale Computing System at the Pittsburgh Supercomputing Center. NSF-CMG Grant No. 0327533 provided partial support for this work.

[1] W.-C. Müller and D. Carati, Phys. Plasmas **9**, 824 (2002).
[2] W.-C. Müller and D. Carati, Comput. Phys. Commun. **147**, 544 (2002).
[3] Y. Ponty, H. Politano, and J.-F. Pinton, Phys. Rev. Lett. **92**, 144503 (2004).
[4] P. D. Mininni, D. C. Montgomery, and A. Pouquet, Phys. Fluids **17**, 035112 (2005).
[5] P. D. Mininni, D. C. Montgomery, and A. Pouquet, Phys. Rev. E **71**, 046304 (2005).
[6] E. N. Parker, *Cosmical Magnetic Fields* (Clarendon Press, New York, 1979).
[7] P. H. Roberts and G. A. Glatzmaier, Geophys. Astrophys. Fluid Dyn. **94**, 47 (2001).
[8] M. Kono and P. H. Roberts, Rev. Geophys. **40**, 1013 (2002).
[9] K. Noguchi, V. I. Pariev, S. A. Colgate, H. F. Beckley, and J. Nordhaus, Astrophys. J. **575**, 1151 (2002).
[10] F. Pétrélis, M. Bourgoin, L. Marié, J. Burguete, A. Chiffaudel, F. Daviaud, S. Fauve, P. Odier, and J.-F. Pinton, Phys. Rev. Lett. **90**, 174501 (2003).
[11] D. R. Sisan, W. L. Shew, and D. P. Lathrop, Phys. Earth Planet. Inter. **135**, 137 (2003).
[12] E. J. Spence, M. D. Nornberg, C. M. Jacobson, R. D. Kendrick, and C. B. Forest, Phys. Rev. Lett. **96**, 055002 (2006).
[13] R. Monchaux *et al.*, Phys. Rev. Lett. **98**, 044502 (2007).
[14] A. A. Schekochihin, S. C. Cowley, J. L. Maron, and J. C. McWilliams, Phys. Rev. Lett. **92**, 054502 (2004).
[15] Y. Ponty, P. D. Mininni, D. C. Montgomery, J.-F. Pinton, H. Politano, and A. Pouquet, Phys. Rev. Lett. **94**, 164502 (2005).
[16] A. Schekochihin, N. Haugen, A. Brandenburg, S. Cowley, J. Maron, and J. McWilliams, Astrophys. J. **625**, L115 (2005).
[17] P. D. Mininni, Y. Ponty, D. C. Montgomery, J.-F. Pinton, H. Politano, and A. Pouquet, Astrophys. J. **626**, 853 (2005).
[18] P. D. Mininni and D. C. Montgomery, Phys. Rev. E **72**, 056320 (2005).
[19] A. B. Iskakov, A. A. Schekochihin, S. C. Cowley, J. C. McWilliams, and M. R. E. Proctor, Phys. Rev. Lett. **98**, 208501 (2007).
[20] D. Vincenzi, J. Stat. Phys. **106**, 1073 (2002).
[21] S. Boldyrev and F. Cattaneo, Phys. Rev. Lett. **92**, 144501 (2004).
[22] A. P. Kazanstev, Sov. Phys. JETP **26**, 1031 (1968).
[23] H. K. Moffatt, *Magnetic Field Generation in Electrically Conducting Fluids* (Cambridge University Press, Cambridge, England, 1978).
[24] A. Pouquet, U. Frisch, and J. Léorat, J. Fluid Mech. **77**, 321 (1976).
[25] M. Meneguzzi, U. Frisch, and A. Pouquet, Phys. Rev. Lett. **47**, 1060 (1981).
[26] A. D. Gilbert, U. Frish, and A. Pouquet, Geophys. Astrophys. Fluid Dyn. **42**, 151 (1988).
[27] A. Brandenburg, Astrophys. J. **550**, 824 (2001).
[28] M. Steenbeck, F. Krause, and K.-H. Rädler, Z. Naturforsch. A **21**, 369 (1966).
[29] F. Krause and K.-H. Rädler, *Mean-field Magnetohydrodynamics and Dynamo Theory* (Pergamon Press, New York, 1980).
[30] S. Childress and A. D. Gilbert, *Stretch, Twist, Fold: The Fast Dynamo* (Springer-Verlag, Berlin, 1995).
[31] B. Galanti, P. L. Sulem, and A. Pouquet, Geophys. Astrophys. Fluid Dyn. **66**, 183 (1992).
[32] Y. Ponty, A. Pouquet, and P. L. Sulem, Geophys. Astrophys. Fluid Dyn. **79**, 239 (1995).
[33] R. Hollerbach, D. J. Galloway, and M. R. E. Proctor, Phys. Rev. Lett. **74**, 3145 (1995).
[34] V. Archontis, S. B. F. Dorch, and A. Nordlund, Astron. Astrophys. **410**, 759 (2003).
[35] P. D. Mininni, Phys. Plasmas **13**, 056502 (2006).
[36] P. Frick, R. Stepanov, and D. Sokoloff, Phys. Rev. E **74**, 066310 (2006).
[37] O. Podvigina and A. Pouquet, Physica D **75**, 471 (1994).
[38] D. D. Holm, Physica D **170**, 253 (2002).
[39] D. D. Holm, Chaos **12**, 518 (2002).
[40] B. J. Geurts and D. D. Holm, J. Turbul. **7**, 1 (2006).
[41] A. Brandenburg and K. Subramanian, Phys. Rep. **417**, 1 (2005).
[42] P. D. Mininni, D. O. Gómez, and S. M. Mahajan, Astrophys. J. **587**, 472 (2003).
[43] A. Alexakis, P. D. Mininni, and A. Pouquet, Phys. Rev. E **72**, 046301 (2005).
[44] P. D. Mininni, A. Alexakis, and A. Pouquet, Phys. Rev. E **72**, 046302 (2005).
[45] U. Müller, R. Stieglitz, and S. Horanyi, J. Fluid Mech. **498**, 31 (2004).
[46] J. Léorat, A. Pouquet, and U. Frisch, J. Fluid Mech. **104**, 419 (1981).
[47] A. Alexakis, P. D. Mininni, and A. Pouquet, Astrophys. J. **640**, 335 (2006).
[48] M. Hossain, W. H. Matthaeus, and D. Montgomery, J. Plasma Phys. **30**, 479 (1983).